EFFECT OF DUST ON Lyα PHOTON TRANSFER IN AN OPTICALLY THICK HALO

YANG YANG[1], ISHANI ROY[2], CHI-WANG SHU[1], AND LI-ZHI FANG[3]
[1] Division of Applied Mathematics, Brown University, Providence, RI 02912, USA
[2] Computing Laboratory, University of Oxford, Oxford, OX1 3QD, UK
[3] Department of Physics, University of Arizona, Tucson, AZ 85721, USA

ABSTRACT

We investigate the effects of dust on Lyα photons emergent from an optically thick medium by solving the integro-differential equation of radiative transfer of resonant photons. To solve the differential equations numerically, we use the weighted essentially non-oscillatory method. Although the effects of dust on radiative transfer are well known, the resonant scattering of Lyα photons makes the problem non-trivial. For instance, if the medium has an optical depth of dust absorption and scattering of $\tau_a \gg 1$, $\tau \gg 1$, and $\tau \gg \tau_a$, the effective absorption optical depth in a random walk scenario would be equal to $\sqrt{\tau_a(\tau_a + \tau)}$. We show, however, that for a resonant scattering at frequency ν_0, the effective absorption optical depth would be even larger than $\tau(\nu_0)$. If the cross section of dust scattering and absorption is frequency-independent, the double-peaked structure of the frequency profile given by the resonant scattering is basically dust-independent. That is, dust causes neither narrowing nor widening of the width of the double-peaked profile. One more result is that the timescales of the Lyα photon transfer in an optically thick halo are also basically independent of the dust scattering, even when the scattering is anisotropic. This is because those timescales are mainly determined by the transfer in the frequency space, while dust scattering, either isotropic or anisotropic, does not affect the behavior of the transfer in the frequency space when the cross section of scattering is wavelength-independent. This result does not support the speculation that dust will lead to the smoothing of the brightness distribution of a Lyα photon source with an optically thick halo.

Key words: cosmology: theory – intergalactic medium – radiative transfer – scattering

1. INTRODUCTION

Lyα photons have been widely applied to study at various epochs of the universe the physics of luminous objects, such as Lyα emitters, Lyα blobs, damped Lyα systems, Lyα forests, fluorescent Lyα emission, star-forming galaxies, quasars at high redshifts, and optical afterglow of gamma-ray bursts (Haiman et al. 2000; Fardal et al. 2001; Dijkstra & Loeb 2009; Latif et al. 2011). The resonant scattering of Lyα photons with neutral hydrogen atoms has a profound effect on the time, space, and frequency dependencies of Lyα photon transfer in an optically thick medium. Lyα photons emergent from an optically thick medium would carry rich information of photon sources and halo surrounding the source of the Lyα photon. The profiles of the emission and absorption of the Lyα radiation are powerful tools for constraining the mass density, velocity, temperature, and the fraction of neutral hydrogen of the optically thick medium. Radiation transfer of Lyα photons in an optically thick medium is fundamentally important.

The radiative transfer of Lyα photons in a medium consisting of neutral hydrogen atoms has been extensively studied both analytically and numerically. However, there have been relatively few results that are directly based on the solutions of the integro-differential equation of the resonant radiative transfer. Besides the Field solution (Field 1959; Rybicki & Dell'Antonio 1994), analytical solutions with and without dust are based mostly on the Fokker–Planck (F–P) approximation (Harrington 1973; Neufeld 1990; Dijkstra et al. 2006). The F–P equation might miss the detailed balance relationship of resonant scattering (Rybicki 2006), and, therefore, the analytical solutions cannot describe the formation and evolution of the Wouthuysen–Field (W–F) local thermalization of the Lyα photon frequency distribution (Wouthuysen 1952; Field 1958), which is important for the emission and absorption of the

hydrogen 21 cm line (e.g., Fang 2009). The features of the Lyα photon transfer related to the W–F local thermalization are also missed. An early effort (Adams et al. 1971) tried to directly solve the integro-differential equation of the resonant radiative transfer with a numerical method. It is still, however, a time-independent approximation.

Recently, a state-of-the-art numerical method has been introduced to solve the integro-differential equation of the radiative transfer with resonant scattering (Qiu et al. 2006, 2007, 2008; Roy et al. 2009a). The solver is based on the weighted essentially non-oscillatory (WENO) scheme (Jiang & Shu 1996). With the WENO solver, many physical features of the transfer of Lyα photons in an optically thick medium (Roy et al. 2009b, 2009c, 2010), which are missed in the F–P equation approximations, have been revealed. For instance, the WENO solution shows that the timescale of the formation of the W–F local thermal equilibrium actually is only about a few hundred times the resonant scattering. It also shows that the double-peaked frequency profile of the Lyα photon emergent from an optically thick medium does not follow the time-independent solutions of the F–P equation. These results directly indicate the need to revisit problems that have been studied only via the F–P time-independent approximation.

We will investigate in this paper the effects of dust on the Lyα photon transfer in an optically thick medium. Dust can be produced at epochs of low and moderate redshifts, and even at redshift as high as 6 (Stratta et al. 2007). Absorption and scattering of dust have been used to explain the observations of Lyα emission and absorption (Hummer & Kunasz 1980), such as the escaping fraction of Lyα photons (Hayes et al. 2010, 2011; Blanc et al. 2011), the redshift dependence of the ratio between Lyα emitters and Lyman break galaxies (Verhamme et al. 2008), and the "evolution" of the double-peaked profile (Laursen et al. 2009).

Nevertheless, it is still unclear whether the timescale of photons escaping from an optically thick halo will be increasing (or decreasing) when the halo is dusty. It is also unclear whether the effects of dust absorption can be estimated by the random walk picture (Hansen & Oh 2006). As for the dust effect on the double-peaked profile, the current results given by different studies seem to be contradictory: some claim that the dust absorption leads to the narrowing of the double-peaked profile (Laursen et al. 2009), while others report that the width between the two peaks apparently should be increasing due to dust absorption (Verhamme et al. 2006). We will focus on these basic problems and examine them with the solution of the integro-differential equation of radiative transfer.

This paper is organized in the following way: Section 2 presents the theory of the Lyα photon transfer in an optically thick medium with dust. The equations of the intensity and flux of resonant photons in a dusty medium are given. We will study three models of the interaction between dust and photons: (1) dust causes only scattering with photons, (2) dust causes both scattering and absorption, and (3) dust causes only absorption of photons. Section 3 gives the solutions of Lyα photons escaping from an optically thick spherical halo with dust. The dusty effect on the double-peaked profile will be studied in Section 4. The discussion and conclusion are given in Section 5. Some mathematical derivations of the equations and numerical implementation details are given in Appendices A and B, respectively.

2. BASIC THEORY

2.1. Radiative Transfer Equation of a Dusty Halo

We study the transfer of Lyα photons in a spherical halo with radius R around an optical source. The halo is assumed to consist of uniformly distributed H I gas and dust. The optical depth of H I scattering over a light path dl is $d\tau = \sigma(\nu)n_{H I}dl$, where $n_{H I}$ is the number density of H I and $\sigma(\nu)$ is the cross section of the resonant scattering of Lyα photons by neutral hydrogen, which is given by

$$\sigma(x) = \sigma_0 \phi(x, a) = \sigma_0 \frac{a}{\pi^{3/2}} \int_{-\infty}^{\infty} dy \frac{e^{-y^2}}{(x - y)^2 + a^2}, \quad (1)$$

where $\phi(x, a)$ is the normalized Voigt profile (Hummer 1965). As usual, the photon frequency ν in Equation (1) is described by the dimensionless frequency $x \equiv (\nu - \nu_0)/\Delta\nu_D$, with $\nu_0 = 2.46 \times 10^{15}$ s^{-1} being the resonant frequency, $\Delta\nu_D = \nu_0(\nu_T/c) = 1.06 \times 10^{11}(T/10^4)^{1/2}$ Hz the Doppler broadening, $\nu_T = \sqrt{2k_B T/m}$ the thermal velocity, and T the gas temperature of the halo. $\sigma_0/\pi^{1/2}$ is the cross section of scattering at the resonant frequency ν_0. The parameter a in Equation (1) is the ratio of natural to Doppler broadening. For the Lyα line, $a = 4.7 \times 10^{-4}(T/10^4)^{-1/2}$. The optical depth of Lyα photons with respect to H I resonant scattering is $\tau_s(x) = n_{H I}R\sigma(x) = \tau_0\phi(x, a)$, where $\tau_0 = n_{H I}\sigma_0 R$.

If the absorption and scattering of dust are described by the effective cross section per hydrogen atom $\sigma_d(x)$, the total optical depth is given by

$$\tau(x) = \tau_0 \phi(x, a) + \tau_d(x), \quad (2)$$

where the dust optical depth $\tau_d(x) = n_{H I}\sigma_d(x)R$. This is equal to assuming that dust is uniformly distributed in the intergalactic medium. The effects of inhomogeneous density distributions of

dust (Neufeld 1991; Haiman & Spaans 1999) will not be studied in this paper.

The radiative transfer equation of Lyα photons in a spherical halo with dust is given by

$$\frac{\partial I}{\partial \eta} + \mu \frac{\partial I}{\partial r} + \frac{(1 - \mu^2)}{r}\frac{\partial I}{\partial \mu} - \gamma \frac{\partial I}{\partial x} = -\phi(x; a)I$$
$$+ \int \mathcal{R}(x, x'; a)I(\eta, r, x', \mu')dx'd\mu'/2 - \kappa(x)I$$
$$+ A\kappa(x) \int \mathcal{R}^d(x, x'; \mu, \mu'; a)I(\eta, r, x', \mu')dx'd\mu' + S,$$
$$(3)$$

where $I(t, r_p, x, \mu)$ is the specific intensity, which is a function of time t, radial coordinate r_p, frequency x, and the direction angle, $\mu = \cos\theta$, with respect to the radial vector **r**.

In Equation (3), we use the dimensionless time η defined as $\eta = cn_{H I}\sigma_0 t$ and the dimensionless radial coordinate r defined as $r = n_{H I}\sigma_0 r_p$. That is, η and r are, respectively, in the units of mean-free flight time and mean-free path of photon ν_0 with respect to the resonant scattering without dust scattering and absorption. Without resonant scattering, a signal propagates in the radial direction with the speed of light; the orbit of the signal is then $r = \eta + $ const. With the dimensionless variable, the size of the halo R is equal to τ_0.

The redistribution function $\mathcal{R}(x, x'; a)$ gives the probability of a photon absorbed at the frequency x' and re-emitted at the frequency x. It depends on the details of the scattering (Henyey & Greestein 1941; Hummer 1962, 1969). If we consider coherent scattering without recoil, the redistribution function with the Voigt profile can be written as

$$\mathcal{R}(x, x'; a) = \frac{1}{\pi^{3/2}} \int_{|x-x'|/2}^{\infty} e^{-u^2}$$
$$\times \left[\tan^{-1}\left(\frac{x_{min} + u}{a}\right) - \tan^{-1}\left(\frac{x_{max} - u}{a}\right)\right] du, \quad (4)$$

where $x_{min} = \min(x, x')$ and $x_{max} = \max(x, x')$. In the case of $a = 0$, i.e., considering only the Doppler broadening, the redistribution function is

$$\mathcal{R}(x, x') = \frac{1}{2} \text{erfc}[\max(|x|, |x'|)]. \quad (5)$$

The redistribution function of Equation (5) is normalized as $\int_{-\infty}^{\infty} \mathcal{R}(x, x')dx' = \phi(x, 0) = \pi^{-1/2}e^{-x^2}$. With this normalization, the total number of photons is conserved in the evolution described by Equation (3). That is, the destruction processes of Lyα photons, such as the two-photon process (Spitzer & Greenstein 1951; Osterbrock 1962), are ignored in Equation (3). The recoil of atoms is also not considered in Equations (4) or (5). The effect of recoil actually is under control (Roy et al. 2009c, 2010). We will address this in the next section.

The absorption and scattering of dust are described by the term $\kappa(x)I$ of Equation (3), where $\kappa(x) = \sigma_d/\sigma_0$, which is of the order of $10^{-8}(T/10^4)^{1/2}$ (Draine & Lee 1984; Draine 2003). The term with A of Equation (3) describes albedo, i.e., $A \equiv \sigma_s/\sigma_d$, where σ_s is the cross section of dust scattering. Generally, A lies approximately between 0.3 and 0.4 (Pei 1992; Weingartner & Draine 2001).

Since dust generally is much heavier than single atoms, the recoil of dust particles can be neglected when colliding with

a photon. Under this "heavy dust" approximation, photons do not change their frequency during the collision with dust. The redistribution function of dust $\mathcal{R}^d$ is independent of x and x', and is simply given by a phase function as

$$\mathcal{R}^d(\mu, \mu') = \frac{1}{4\pi} \int_0^{2\pi} d\phi' \frac{1 - g^2}{(1 + g^2 - 2g\bar{\mu})^{3/2}}$$
$$= \sum_{l=0}^{\infty} \frac{(2l+1)}{2} g^l P_l(\mu) P_l(\mu'), \qquad (6)$$

where $\bar{\mu} = \mu\mu' + \sqrt{(1 - \mu^2)(1 - \mu'^2)}\cos\phi'$ and P_l is the Legendre function. The factor g in Equation (6) is the asymmetry parameter. For isotropic scattering, $g = 0$. The cases of $g = +1$ and -1 correspond to complete forward and backward scattering, respectively. Generally, the factor g is a function of the wavelength. For the Lyα photon, we will take $g = 0.73$ for realistic dust scattering (Li & Draine 2001). The integral of Equation (6) is performed in Appendix A.

In Equation (3), the term with the parameter γ is due to the expansion of the universe. If n_H is equal to the mean of the number density of cosmic hydrogen, we have $\gamma = \tau_{GP}^{-1}$, and τ_{GP} is the Gunn–Peterson optical depth. Since the Gunn–Peterson optical depth is of the order of 10^6 at high redshift (e.g., Roy et al. 2009c), the parameter γ is of the order of 10^{-5} to 10^{-6}. Therefore, if the optical depth of halos is equal to or less than 10^6, the term with γ of Equation (3) can be ignored.

In Equation (3), we neglect the effect of collision transition from the H($2p$) state to the H($2s$) state, which can significantly affect the escape of Lyα photons when the H I column density is higher than 10^{21} cm^{-2} and the dust absorption is very small (Neufeld 1990). This is generally out of the parameter range used below. We are also not considering the effects of bulk motion of the medium of halos (e.g., Spaans & Silk 2006; Xu & Wu 2010).

2.2. Eddington Approximation

Equation (6) indicates that the transfer equation (3) can be solved with the Legendre expansion $I(\eta, r, x, \mu) = \sum_l I_l(\eta, r, x) P_l(\mu)$. If we take only the first two terms, $l = 0$ and 1, it is the Eddington approximation as

$$I(\eta, r, x, \mu) \simeq J(\eta, r, x) + 3\mu F(\eta, r, x), \qquad (7)$$

where

$$J(\eta, r, x) = \frac{1}{2} \int_{-1}^{+1} I(\eta, r, x, \mu) d\mu,$$
$$F(\eta, r, x) = \frac{1}{2} \int_{-1}^{+1} \mu I(\eta, r, x, \mu) d\mu. \qquad (8)$$

They are, respectively, the angularly averaged specific intensity and flux. Defining $j = r^2 J$ and $f = r^2 F$, Equation (3) yields the equations of j and f as

$$\frac{\partial j}{\partial \eta} + \frac{\partial f}{\partial r} = -(1 - A)\kappa j - \phi(x; a)j + \int \mathcal{R}(x, x'; a)j dx'$$
$$+ \gamma \frac{\partial j}{\partial x} + r^2 S, \qquad (9)$$

$$\frac{\partial f}{\partial \eta} + \frac{1}{3}\frac{\partial j}{\partial r} - \frac{2}{3}\frac{j}{r} = -(1 - Ag)\kappa f + \gamma \frac{\partial f}{\partial x} - \phi(x; a)f. \quad (10)$$

The mean intensity $j(\eta, r, x)$ describes the x photons trapped in the position r at time η by the resonant scattering, while the flux $f(\eta, r, x)$ describes the photons in transit.

The source term S in Equations (3) and (9) can be described by a boundary condition of j and f at $r = r_0$. We can take $r_0 = 0$. Thus, the boundary condition is

$$j(\eta, 0, x) = 0, \quad f(\eta, 0, x) = S_0\phi_s(x), \qquad (11)$$

where S_0 and $\phi_s(x)$ are, respectively, the intensity and normalized frequency profile of the sources. Since Equation (3) is linear, the solutions of $j(x)$ and $f(x)$ for a given $S_0 = S$ are equal to $Sj_1(x)$ and $Sf_1(x)$, where $j_1(x)$ and $f_1(x)$ are the solutions of $S_0 = 1$. On the other hand, Equation (3) is not linear with respect to the function $\phi_s(x)$. The solution $f(x)$ for a given $\phi_s(x)$ is not equal to $\phi_s(x)f_1(x)$, where $f_1(x)$ is the solution of $\phi_s(x) = 1$.

In the range outside the halo, $r > R$, no photons propagate in the direction $\mu < 0$. The boundary condition at $r = R$ given by $\int_0^{-1} \mu J(\eta, R, x, \mu) d\mu = 0$ is then (Unno 1955)

$$j(\eta, R, x) = 2f(\eta, R, x). \qquad (12)$$

There is no photon in the field before $t = 0$. Therefore, the initial condition is

$$j(0, r, x) = f(0, r, x) = 0. \qquad (13)$$

We will solve Equations (9) and (10) with boundary and initial conditions given by Equations (11)–(13) by using the WENO solver (Roy et al. 2009a, 2009b, 2009c, 2010). Some details of this method are given in Appendix B.

2.3. Dust Models

We consider three models of the dust as follows:

I. *Pure scattering.* $A = 1$, $g = 0.73$: dust causes only anisotropic scattering, but no absorption.
II. *Scattering and absorption.* $A = 0.32$, $g = 0.73$: dust causes both absorption and anisotropic scattering.
III. *Pure absorption.* $A = 0$: dust causes only absorption, but no scattering.

Models I and III do not occur in reality. They are, however, helpful to reveal the effects of pure scattering and absorption on the radiative transfer.

Since $\kappa(x)$ is on the order of 10^{-8}, its effect will be significant only for halos with optical depth $\tau_0 \geqslant 10^6$, and ignorable for $\tau_0 \leqslant 10^5$. To illustrate the dust effect, we use halos of $R = \tau_0 \leqslant 10^4$ and take larger κ to be $\simeq 10^{-4}$ to 10^{-2}. We also assume that κ is frequency-independent. We consider below only the case of gray dust, i.e., κ is independent of the frequency x. This is certainly not realistic dust. However, the frequency given in the solutions below mostly is in the range $|x| < 4$. Therefore, the approximation of gray dust would be proper if the cross section of dust is not significantly frequency-dependent in the range $|x| < 4$.

2.4. Numerical Example: Wouthuysen–Field Thermalization

As the first example of numerical solutions, we show the W–F effect, which requires that the distribution of Lyα photons in the frequency space should be thermalized near the resonant frequency ν_0. The W–F effect illustrates the difference between the analytical solutions of the F–P approximation
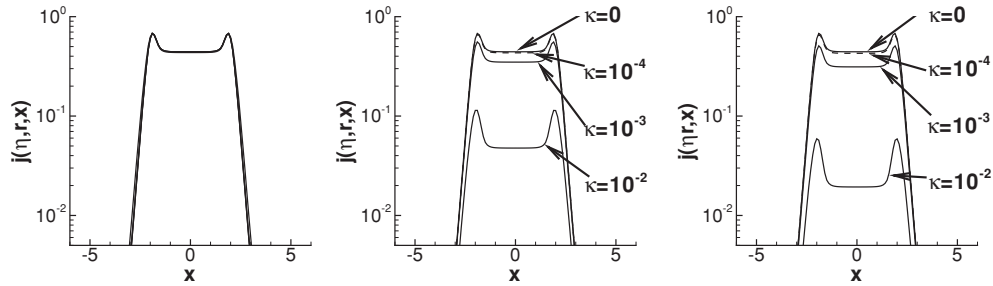
Figure 1. Mean intensity $j(\eta, r, x)$ at $\eta = 500$ and $r = 100$ for dust models I (left panel), II (middle panel), and III (right panel). The source is $S_0 = 1$ and $\phi_s(x) = (1/\sqrt{\pi})e^{-x^2}$. The parameter $a = 10^{-3}$. In each panel, κ is taken to be 0, 10^{-4}, 10^{-3}, and 10^{-2}.
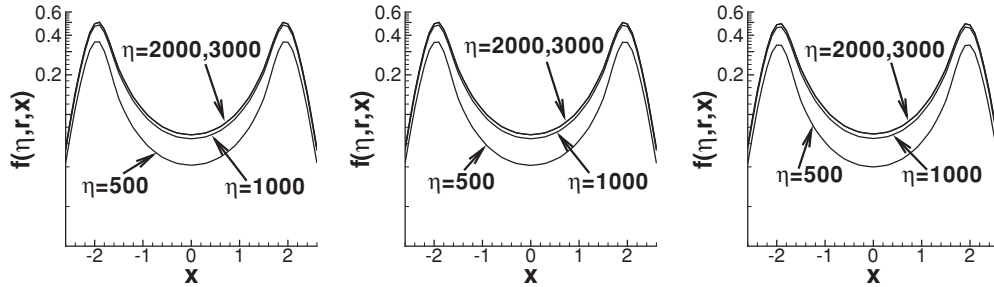
Figure 2. Flux $f(\eta, r, x)$ of Lyα photons emergent from halos at the boundary $R = 10^2$, and for the dust model I, $A = 1$, $g = 0.73$. The parameter κ is taken to be 10^{-4} (left), 10^{-3} (middle), and 10^{-2} (right). The source is $S_0 = 1$ and $\phi_s(x) = (1/\sqrt{\pi})e^{-x^2}$. The parameter $a = 10^{-3}$.

and those of Equations (9) and (10). The former cannot show the local thermalization (Neufeld 1990), while the latter can (Roy et al. 2009b). All problems related to the W–F local thermal equilibrium should be studied with the integro-differential equation (Equation (3)).

Figure 1 presents a solution of mean intensity $j(\eta, r, x)$ at time $\eta = 500$ and radial coordinate $r = 10^2$ for a halo with size $R \gg r = 10^2$. The three panels correspond to dust models I (left panel), II (middle panel), and III (right panel). The source is taken to have a Gaussian profile $\phi_s(x) = (1/\sqrt{\pi})e^{-x^2}$ and unit intensity $S_0 = 1$. The solutions of Figure 1 are actually independent of R, if $R \gg 10^2$. The intensity of j is decreasing from left to right in Figure 1, because the absorption is increasing with the models from I to III.

A remarkable feature shown in Figure 1 is that all $j(\eta, r, x)$ have a flat plateau in the range $|x| \leqslant 2$. This gives the frequency range of the W–F local thermalization (Roy et al. 2009b, 2009c). The range of the flat plateau $|x| \leqslant 2$ is almost dust-independent, either for model I or for models II and III. This is expected, as neither the absorption nor scattering given by the κ term of Equation (3) changes the frequency distribution of photons. The redistribution function (Equation (6)) also does not change the frequency distribution of photons. This point can also be seen from Equations (9) and (10), in which the κ terms are frequency-independent. The evolution of the frequency distribution of photons is due only to the resonant scattering.

Since thermalization will erase all frequency features within the range $|x| \leqslant 2$, the double-peaked structure does not retain information of the photon frequency distribution within $|x| < 2$ at the source. That is, the results in Figure 1 will hold for any source $S_0\phi_s(x)$ with arbitrary $\phi_s(x)$ that is non-zero within $|x| < 2$ (Roy et al. 2009b, 2009c). This property can also be used as a test of the simulation code. It requires that the simulation results of the flat plateau should hold, regardless of whether the source is monochromatic or has finite width around ν_0.

## 3. DUST EFFECTS ON PHOTON ESCAPE

3.1. Model I: Scattering of Dust

To study the effects of dust scattering on the Lyα photon escape, we show in Figure 2 the flux $f(\eta, r, x)$ of Lyα photons emergent from halos at the boundary $r = R = 10^2$ for Model I. The three panels of Figure 2 correspond to $\kappa = 10^{-4}$, 10^{-3}, and 10^{-2} from left to right, respectively. The source starts to emit photons at $\eta = 0$ with a stable luminosity $S_0 = 1$ and with a Gaussian profile $\phi_s(x) = (1/\sqrt{\pi})e^{-x^2}$.

Figure 2 clearly shows that the time evolution of $f(\eta, r, x)$ is κ-independent. Although the cross section of dust scattering increases by about 100 times from $\kappa = 10^{-4}$ to $\kappa = 10^{-2}$, the curves of the left and right panels in Figure 2 are actually almost identical.

According to the scenario of "single longest excursion," the photon escape is not a process of Brownian random walk in the spatial space, but rather a transfer in the frequency space (Osterbrock 1962; Avery & House 1968; Adams 1972, 1975; Harrington 1973; Bonilha et al. 1979). A photon will escape once its frequency is transferred from $|x| < 2$ to $|x| > 2$, on which the medium is transparent. On the other hand, dust scattering given by the redistribution function equation (Equation (6)) does not change photon frequency. Dust scattering has no effect on the transfer in the frequency space.

Moreover, photons with frequency $|x| < 2$ are quickly thermalized after a few hundred resonant scattering. In the local thermal equilibrium state, the angular distribution of photons is isotropic. Thus, even if the dust scattering is anisotropic $g \neq 0$ with respect to the direction of the incident particle, the angular distribution will keep isotropic undergoing a $g \neq 0$ scattering. Hence, dust scattering also has no effect on the angular distribution.

4
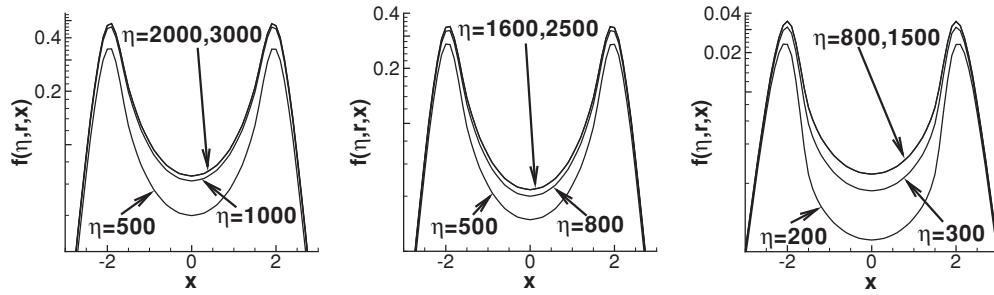
Figure 3. Flux $f(\eta, r, x)$ of Lyα photons emergent from halos at the boundary $r = R = 10^2$. The parameters of the dust are $A = 0$ and $\kappa = 10^{-4}$ (left), 10^{-3} (middle), and 10^{-2} (right). Other parameters are the same as those in Figure 2.
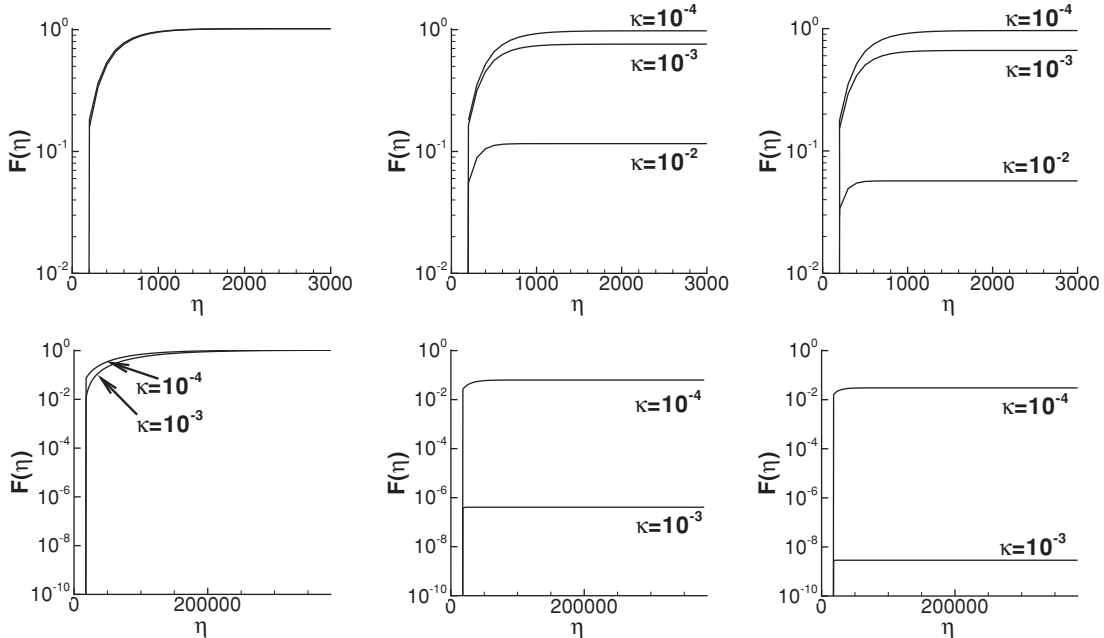
Figure 4. Time evolution of the total flux $F(\eta)$ at the boundary of halos with $R = \tau_0 = 10^2$ (upper panels) and $R = \tau_0 = 10^4$ (lower panels). The source of $S_0 = 1$ and $\phi_s(x) = (1/\sqrt{\pi})e^{-x^2}$ starts to emit photons at time $\eta = 0$. The parameters of dust are $(A = 1, g = 0.73)$ (left), $(A = 0.32, g = 0.73)$ (middle), and $A = 0$ (right). In each panel of $R = 10^2$, κ is taken to be 10^{-4}, 10^{-3}, and 10^{-2}. In the cases of $R = 10^4$, κ is taken to be 10^{-4} and 10^{-3}.

3.2. Model III: Absorption of Dust

Similar to Figure 2, we present in Figure 3 the flux of Model III, i.e., dust causes only absorption without scattering. All other parameters of Figure 3 are the same as in Figure 2. In the left panel of Figure 3, the curves at the time $\eta = 2000$ and 3000 are the same. This means the flux $f(\eta, R, x)$ at the boundary R is already stable, or saturated at the time $\eta \geqslant 2000$. The small difference between the curves of $\eta = 1000$ and $\eta \geqslant 2000$ of the left panel indicates that the flux is still not yet completely saturated at the time $\eta = 1000$. However, comparing the middle and right panels of Figure 3, we see that for $\kappa = 10^{-3}$, the flux has already saturated at $\eta = 1600$, while it has saturated at $\eta = 800$ for $\kappa = 10^{-2}$. That is, the stronger the dust absorption, the shorter the saturation timescale. The timescales of escape or saturation do not increase by dust absorption, and even decrease with respect to the medium without dust. Stronger absorption leads to a shorter timescale of saturation.

Obviously, dust absorption does not help in producing photons for the "single longest excursion." Therefore, dust absorption cannot make the timescale of producing photons for the "single longest excursion" smaller. However, dust absorptions are effective in reducing the number of photons trapped in the state of local thermalized equilibrium $|x| < 2$ (see also

Section 4.2). This leads to the fact that the higher the value of κ, the shorter the timescale of saturation.

3.3. Effective Absorption Optical Depth

Since Lyα photons underwent a large number of resonant scattering before escaping from the halo with optical depth $\tau_0 \gg 1$, it is generally believed that a small absorption of dust will lead to a significant decrease of the flux. However, it is still unclear what the exact relationship between the dust absorption and the resonant scattering is. This problem should be measured by the effective optical depth of dust absorption of Lyα photons in $R = \tau_0 \gg 1$ halos.

To calculate the effective optical depth, we first give the total flux of Lyα photons emergent from the halo of radius R, which is defined as $F(\eta) = \int f(\eta, R, x)dx$. Figure 4 plots $F(\eta)$ as a function of time η for a halo with sizes $R = \tau_0 = 10^2$ and 10^4. The curves typically are the time evolution of growing and then saturating. The three panels correspond to the dust models I, II, and III from left to right. The upper panels are of $R = 10^2$, and the lower panels are of $R = 10^4$. In each panel of $R = 10^2$, we have three curves corresponding to $\kappa = 10^{-4}$, 10^{-3}, and 10^{-2}, respectively. In cases of $R = 10^4$, we take $\kappa = 10^{-4}$ and 10^{-3}.

Table 1
Effective Absorption Optical Depth τ_{effect}

Dust Effect on Lyα Photon Transfer			Model II			Model III	
$R = \tau_0$	κ	τ_a	f_S	τ_{effect}	τ_a	f_S	τ_{effect}
10^2	10^{-4}	0.0068	0.978	2.2×10^2	0.01	0.963	3.8×10^2
10^2	10^{-3}	0.068	0.760	2.7×10^2	0.10	0.670	4.0×10^2
10^2	10^{-2}	0.68	0.116	2.2×10^2	1.00	0.057	2.9×10^2
10^4	10^{-4}	0.68	6.28×10^{-2}	2.8×10^4	1.00	3.02×10^{-2}	3.5×10^4
10^4	10^{-3}	6.8	4.07×10^{-7}	1.5×10^4	10.0	2.87×10^{-9}	1.97×10^4

The left panel of Figure 4 shows that the three curves of $\kappa = 10^{-4}, 10^{-3}$, and 10^{-2} are almost the same. This is consistent with Figure 2 for model I in that the time evolution of f is κ-independent for the pure scattering dust. For the pure absorption dust (the right panel of Figure 4), the saturated flux is smaller for larger κ. We can also see from Figure 4 that the timescale of approaching saturation is smaller for larger κ. The result of model II is in between that for models I and III.

With the saturated flux of Figure 4, one can define the effective absorption optical depth by $\tau_{effect} \equiv -(1/\kappa) \ln f_S$. The results are shown in Table 1, in which τ_a is the dust absorption depth. It is interesting to see that the effective absorption optical depth is always equal to about a few times of the optical depth of resonant scattering τ_0, regardless of whether τ_a is less than 1. Namely, the effective absorption depth τ_{effect} of dust is roughly proportional to τ_0.

According to the random walk scenario, if a medium has optical depths of absorption τ_a and scattering τ_s, the effective absorption optical depth should be equal to $\tau_{effect} = \sqrt{\tau_a(\tau_a + \tau_s)}$ (Rybicki & Lightman 1979, p. 393). However, the results of the last line of Table 1 show that the random walk scenario does not work for the dust effect on resonant photon transfer. This result is consistent with Figures 2 and 3. When the optical depth of dust is lower than the optical depth of resonant scattering τ_0, the timescale of photon escaping basically is not affected by the dust, but is proportional to τ_0; therefore, the absorption is also proportional to τ_0.
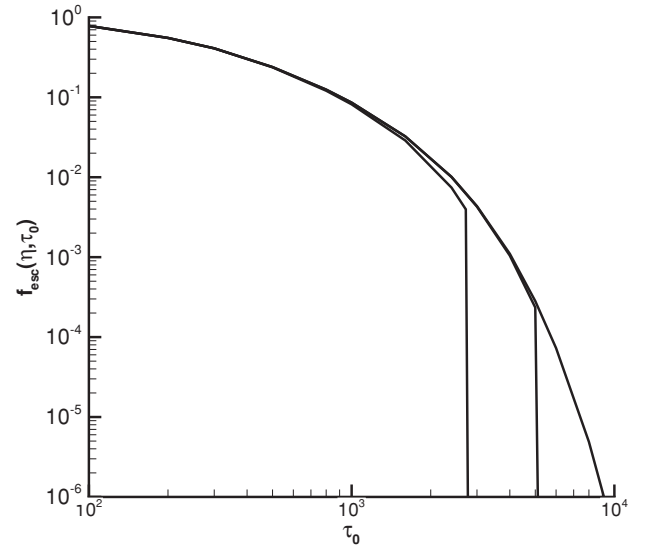
3.4. Escape Coefficient

With the total flux, we can define the escaping coefficient of the Lyα photon as $f_{esc}(\eta, \tau_0) \equiv F(\eta)/F_0$, where F_0 is the flux of the center source. Figure 5 shows $f_{esc}(\eta, \tau_0)$ at three times $\eta = 5 \times 10^3, 10^4$, and 3.2×10^4 for Model II and $\kappa = 10^{-3}$. At $\eta = 5 \times 10^3$, the flux of halos with $\tau_0 \leqslant 10^3$ is saturated. At $\eta = 10^4$, halos with $\tau_0 \leqslant 3 \times 10^3$ are saturated, and all halos of $\tau_0 \leqslant 10^4$ are saturated at $\eta = 3.2 \times 10^4$.

4. DUST EFFECTS ON THE DOUBLE-PEAKED PROFILE

4.1. Dust and the Frequency of Double Peaks

A remarkable feature of Lyα photon emergent from optically thick medium is the double-peaked profile. Figures 1–3 have shown that the double peak frequencies $x_+ = |x_-|$ are almost independent of either the scattering or the absorption of dust. In this section, we consider halos with size R or τ_0 larger than 10^2. Figure 6 presents the double peak frequency $|x_\pm|$ as a function of $a\tau_0$, where the parameter a is taken to be 10^{-2} (left) and 5×10^{-3} (right). Comparing the curves with and without dust in Figure 6, we can say that the dust effect on $|x_\pm|$ is very small until $a\tau_0 = aR = 10^2$.

In the range $a\tau_0 < 20$, the $|x_\pm|-\tau_0$ relation is almost flat with $|x_\pm| \simeq 2$. This is because the double-peaked profile is

**Figure 5.** Escaping coefficient $f_{esc}(\eta)$ as a function of the optical depth τ_0 of halo at time $\eta = 5 \times 10^3, 10^4$, and 3.2×10^4 from bottom to up. Dust is modeled by II, $A = 0.32$, $g = 0.73$, and $\kappa = 10^{-3}$.

given by the frequency range of the locally thermal equilibrium. The positions of the two peaks, x_+ and x_-, are basically at the maximum and minimum frequencies of the local thermalization. The frequency range of the local thermal equilibrium state is mainly determined by the Doppler broadening and is weakly dependent on τ_0. Thus, we always have $x_\pm \simeq \pm 2$. When the optical depth is larger, $a\tau_0 \sim 10^2$, more and more photons of the flux are attributed to the resonant scattering by the Lorentzian wing of the Voigt profile. In this phase, $|x_\pm|$ will increase with τ_0.

Figure 6 also shows a line $x_\pm = \pm(a\tau_0)^{1/3}$, which is given by the analytical solution of the F–P approximation, in which the Doppler broadening core in the Voigt profile is ignored (Harrington 1973; Neufeld 1990; Dijkstra et al. 2006). The numerical solutions of Equations (3) or (9) and (10) deviate from the $(a\tau_0)^{1/3}$-law at all parameter range of Figure 6. The deviation at $a\tau_0 < 20$ is due to the fact that the Doppler broadening core in the Voigt profile is ignored in the F–P approximation; no locally thermal equilibrium can be reached. Therefore, in the range $a\tau_0 < 20$, $|x_\pm|$ of the WENO solution is larger than the $(a\tau_0)^{1/3}$-law. In the range of $a\tau_0 > 20$, the F–P approximation yields a faster diffusion of photons in the frequency space. This point can be seen in the comparison between an F–P solution with Field's analytical solution (Figure 1 in Rybicki & Dell'Antonio 1994). In this range, the numerical results of $|x_\pm|$ are less than the $(a\tau_0)^{1/3}$-law.

4.2. No Narrowing and No Widening

The dust effect has been used to explain the narrowing of the width between the two peaks (Laursen et al. 2009). Oppositely, it
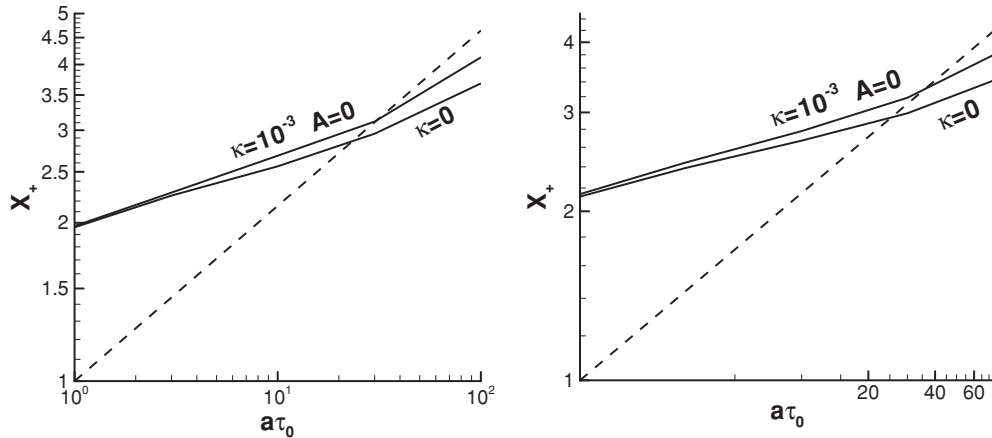
Figure 6. Two-peak frequencies $x_+ = |x_-|$ as a function of $a\tau_0$. The parameter a is taken to be 10^{-2} (left) and 5×10^{-3} (right). Dust model III (pure absorption) is used, and κ is taken to be 10^{-3}. The dashed straight line gives $\log x_{\pm}$–$\log a\tau$ with slope 1/3, which is to show the $(a\tau)^{1/3}$-law of $x_{\pm}$.

is also used to explain the widening of the width between the two peaks (Verhamme et al. 2006). However, Figures 1, 2, 3, and 6 already show that the width between the two peaks of the profile is very weakly dependent on dust scattering and absorption. This result supports, at least in the parameter range considered in Figures 1–3, neither the narrowing nor the widening of the two peaks.

If dust absorption can cause narrowing, the absorption should be weaker at $|x| \sim 0$ and stronger at $|x| \geqslant 2$. Similarly, if dust absorption can cause widening, the absorption should be weaker at $|x| \sim 2$ and stronger at $|x| \sim 0$. To test these assumptions, Figure 7 plots $\ln[f(\eta, r, x, \kappa = 0)/f(\eta, r, x, \kappa)]$ as a function of x. It measures the x(frequency) dependence of the flux ratio with and without dust absorption. We take large η, and then the fluxes in Figure 7 are saturated. Figure 7 shows that the absorption in the range $|x| < 2$ is much stronger than that in $|x| > 2$; therefore, the assumption of the narrowing is ruled out. Figure 7 also shows that the curves of $\ln[f(\eta, r, x, \kappa = 0)/f(\eta, r, x, \kappa = 10^{-3})]$ are almost flat in the range $|x| < 2$. Therefore, the assumption of widening of the two peaks can also be ruled out.

The cross sections of dust absorption and scattering are assumed to be frequency-independent. Equations (9) and (10) do not contain any frequency scales other than that from resonant scattering. However, either narrowing or widening would require frequency scales different from those of resonant scattering. This occurrence is not possible if the dust is gray.

4.3. Profile of Absorption Spectrum

If the radiation from the sources has a continuum spectrum, the effect of neutral hydrogen halos is to produce an absorption line at $\nu = \nu_0$. The profile of the absorption line can also be found by solving Equations (9) and (10), replacing the boundary equation (Equation (11)) by

$$j(\eta, 0, x) = 0, \quad f(\eta, 0, x) = S_0. \quad (14)$$

That is, we assume that the original spectrum is flat in the frequency space. The spectrum of the flux emergent from the halo of $R = 10^2$ and 10^4 with the central source of Equation (14) for dust models I, II, and III is shown in Figure 8. All curves are for large η, i.e., they are saturated.

The optical depths at the frequency $|x| > 4$ are small; therefore, the Eddington approximation might no longer be proper. However, those photons do not strongly involve the

resonant scattering; hence, they do not significantly affect the solution around $x = 0$. The solutions of Figure 8 are still useful for studying the profiles of f around $x = 0$.

The flux profiles of Figure 8 are typically absorption lines with width given by the double peaks similar to the double-peaked structure of the emission line. The flux at the double peaks is even higher than that at the flat wing. This is because more photons are stored in the frequency range $|x| < 2$. According to the redistribution function equation (Equation (4)), the probability of transferring an x' photon to an $|x| < |x'|$ photon is greater than that from $|x'|$ to $|x| > |x'|$. Therefore, if the original spectrum is flat, the net effect of resonant scattering is to bring photons with frequency $|x| > 2$ to $|x| < 2$. Photons stored at $|x| < 2$ are thermalized; therefore, in the range $|x| < 2$, the profile will be the same as the emission line and the double peaks can be higher than the wing. This puts the shoulder at $|x| \sim 2$.

As expected, for model I (left panels of Figure 8), the double profile is completely κ-independent. Dusty scattering does not change the flux and its profile. For models II and III, the higher the κ, the lower the flux of the wing because the dust absorption is assumed to be frequency-independent. The positions of the double peaks, x, in the absorption spectrum are also κ-independent. This once again shows that dust absorption and scattering cause neither narrowing nor widening of the double-peaked profile. However, for higher κ the flux of the peaks is lower. When the absorption is very strong, the double-peaked structure might disappear, but will never be narrowed or widened.

5. DISCUSSIONS AND CONCLUSIONS

The study of dust effects on radiative transfer has had a long history related to extinction. However, dust effects on radiative transfer of resonant photons actually have not been carefully investigated. Existing works are based mostly on the solutions of the F–P approximation or Monte Carlo simulation. These results are important. We revisited these problems with the WENO solver of the integro-differential equation of the resonant radiative transfer and have found some features that have not been addressed in previous work. These features are summarized as follows.

First, the random walk picture in the physical space will no longer be available for estimating the effective optical depth of dust absorption. For a medium with optical depth of absorption and resonant scattering of $\tau_a \gg 1$ $\tau(\nu_0) \gg 1$ and
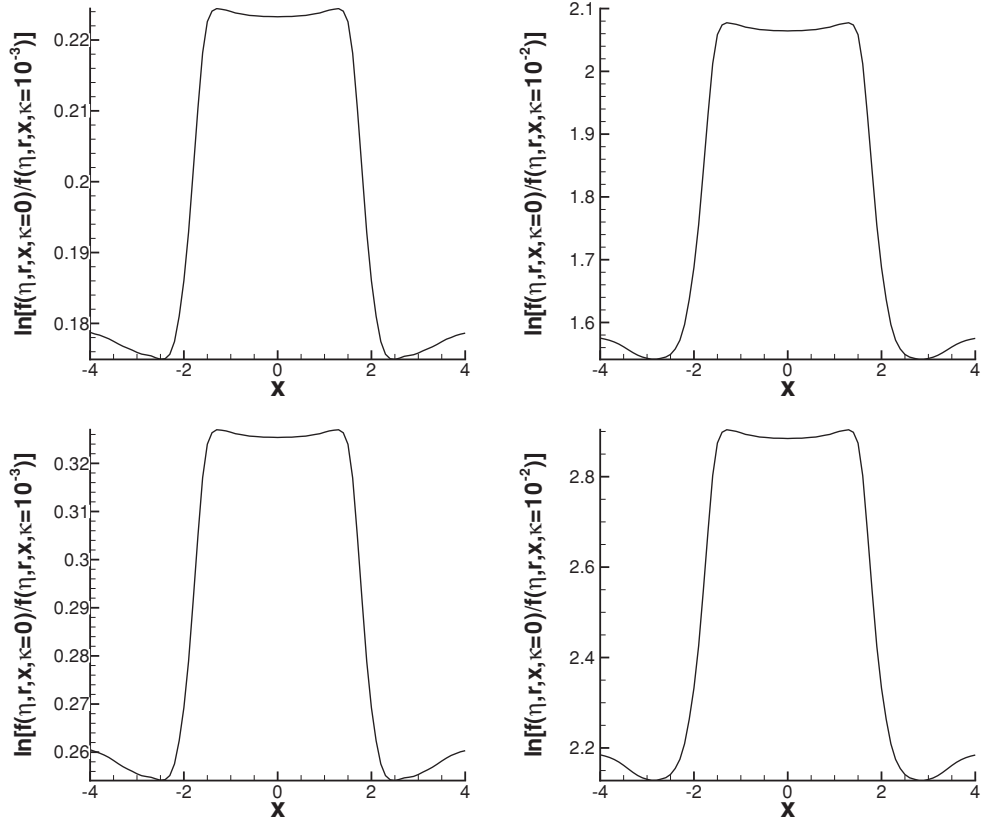
Figure 7. $\ln[f(\eta, r, x, \kappa = 0)/f(\eta, r, x, \kappa)]$ as a function of x for models II (top) and III (bottom), and $\kappa = 10^{-3}$ (left) and 10^{-2} (right). Other parameters are the same as those in Figure 2.
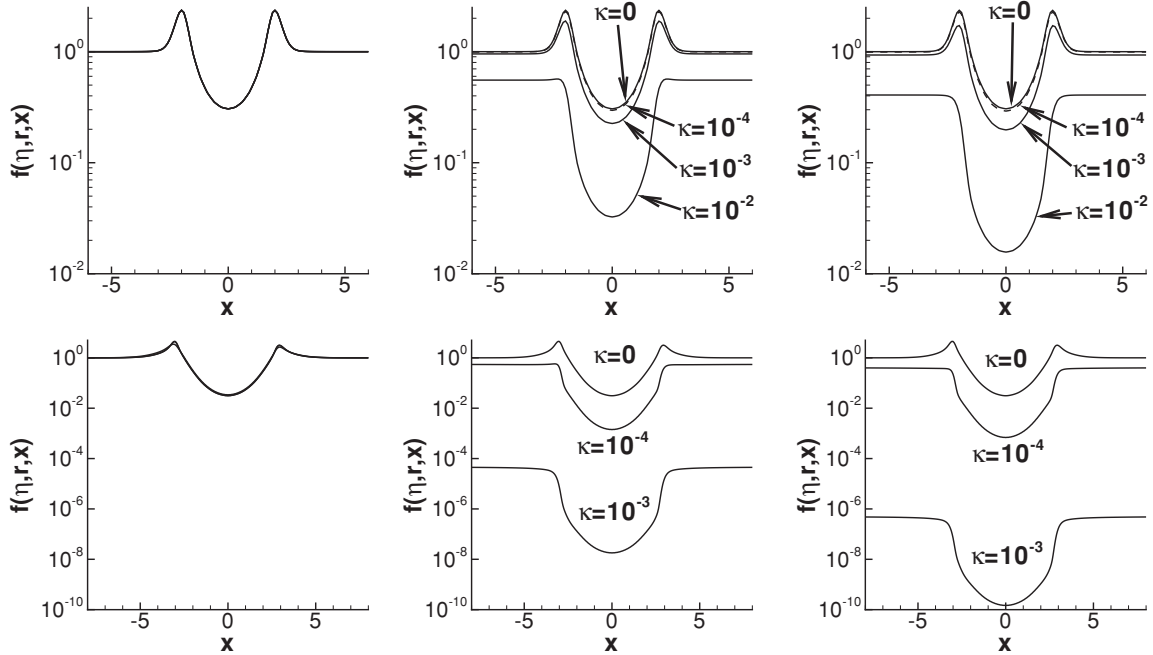
Figure 8. Spectrum of the flux emergent from the halo of $R = 10^2$ (upper panels) and 10^4 (lower panels) with central source of Equation (14) for the dust models I (left), II (middle), and III (right). Other parameters are the same as those in Figure 2.

$\tau_s(\nu_0) \gg \tau_a$, the effective absorption optical depth is found to be almost independent of τ_a, and equal to about a few times of $\tau_s(\nu_0)$.

Second, dust absorption will, of course, yield the decrease of the flux of Lyα photons emergent from the optically thick medium. However, if the absorption cross section of dust is frequency-independent, the double-peaked structure of the frequency profile is basically dust-independent. The double-peaked structure does not get narrowed or widened by the absorption and scattering of dust.

Third, the timescales of Lyα photon transfer are basically independent of dust scattering and absorption. This is because those timescales are mainly determined by the kinetics in the frequency space, while dust does not affect the behavior of the transfer in the frequency space if the cross section of the dust is wavelength-independent. The local thermal equilibrium makes the anisotropic scattering ineffective on the angular distribution of photons. Dust absorption and scattering do not lead to the increase or decrease of the time of storing Lyα photons in the halos.

The difference between the time-independent solutions of the F–P approximation or Monte Carlo simulation and the WENO solution of Equation (3) is mainly related to the W–F effect. Therefore, all above-mentioned features can already be clearly seen with halos of $\tau_0 \sim 10^2$, in which the W–F local thermal equilibrium has been well established.

In this context, most of the calculations in this paper are on holes with $\tau_0 < 10^5$. This range of τ_0 certainly is unable to describe halos with column number density of H I larger than 10^{17} cm^{-2} (e.g., Roy et al. 2010). Nevertheless, the result of $\tau_0 < 10^5$ would already be useful for studying the 21 cm region around high-redshift sources, of which the optical depth typically is (Liu et al. 2007; Roy et al. 2009c)

$$\tau_0 = 3.9 \times 10^5 f_{\rm H I} \left(\frac{T}{10^4 \ {\rm K}} \right)^{-1/2} \left(\frac{1+z}{10} \right)^3$$
$$\times \left(\frac{\Omega_b h^2}{0.022} \right) \left(\frac{R_{\rm ph}}{10 \ {\rm kpc}} \right), \quad (15)$$

where $f_{\rm H I}$ is the fraction of H I. All other parameters in Equation (15) are taken from the concordance ΛCDM mode. For these objects the relation between dimensionless η and physical time t is given by

$$t = 5.4 \times 10^{-2} f_{\rm H I}^{-1} \left(\frac{T}{10^4 \ {\rm K}} \right)^{1/2} \left(\frac{1+z}{10} \right)^{-3} \left(\frac{\Omega_b h^2}{0.022} \right)^{-1} \eta, \ {\rm yr}.$$
$$(16)$$

The 21 cm emission relies on the W–F effect. On the other hand, the timescale of the evolution of the 21 region is short. The effect of dust on the timescales of Lyα evolution should be considered.

We have not considered the Lyα photons produced by the recombination in an ionized halo. If a halo is optically thick, photons from the recombination will also be thermalized. The information of where the photon comes from will be lost during the thermalization. Therefore, photons from recombination should not show any difference from those emitted from central sources. Only the photons formed at the place very close to the boundary of the halo will not be thermalized and may yield different behavior.

APPENDIX A

INTEGRAL OF THE PHASE FUNCTION (Equation (6))

Equation (6) can be rewritten as

$$\mathcal{R}^d(\mu, \mu') = \frac{1}{4\pi} \int_0^{2\pi} d\phi' \frac{1-g^2}{|{\bf I} - g{\bf I'}|^{\frac{3}{2}}}, \quad (A1)$$

where **I** and **I′** are unit vector on the direction of polar angle θ and θ', and azimuth angle ϕ and ϕ', respectively. That is $\mathbf{I} \cdot \mathbf{I} = \mathbf{I'} \cdot \mathbf{I'} = 1$ and $\mathbf{I} \cdot \mathbf{I'} = \cos\gamma = \cos\theta \cos\theta' + \sin\theta \sin\theta' \cos(\phi - \phi')$, and $\mu = \cos\theta$, $\mu' = \cos\theta$. We have

$$\frac{d}{dg} \frac{1}{|{\bf I} - g{\bf I'}|^{1/2}} = \frac{1-g^2}{2g|{\bf I} - g{\bf I'}|^{3/2}} - \frac{1}{2g|{\bf I} - g{\bf I'}|^{1/2}}, \quad (A2)$$

and therefore,

$$\frac{1-g^2}{|{\bf I} - g{\bf I'}|^{3/2}} = 2g \frac{d}{dg} \frac{1}{|{\bf I} - g{\bf I'}|^{1/2}} + \frac{1}{|{\bf I} - g{\bf I'}|^{1/2}}. \quad (A3)$$

The expansion with Legendre functions $P_l(\cos\gamma)$ gives

$$\frac{1}{|{\bf I} - g{\bf I'}|^{1/2}} = \sum_{l=0}^{\infty} g^l P_l(\cos\gamma), \quad (A4)$$

and then

$$\frac{1-g^2}{|{\bf I} - g{\bf I'}|^{3/2}} = \sum_{l=1}^{\infty} 2l g^l P_l(\cos\gamma) + \sum_{l=0}^{\infty} g^l P_l(\cos\gamma). \quad (A5)$$

Since $\cos\gamma = \cos\theta \cos\theta' + \sin\theta \sin\theta' \cos(\phi - \phi')$, we have the following identity for the Legendre function $P_l(\cos\gamma)$:

$$P_l(\cos\gamma) = P_l(\cos\theta) P_l(\cos\theta') + 2 \sum_{m=1}^{m=l} \frac{(l-m)!}{(l+m)!}$$
$$\times P_l^m(\cos\theta) P_l^m(\cos\theta') \cos[m(\phi - \phi')]. \quad (A6)$$

The integral of ϕ' in Equation (A1) kills the second term of Equation (A6); we then have

$$\mathcal{R}^d(\mu, \mu') = \frac{1}{4\pi} 2\pi \left[\sum_{l=1}^{\infty} 2l g^l P_l(\cos\theta) P_l(\cos\theta') \right.$$
$$\left. + \sum_{l=0}^{\infty} g^l P_l(\cos\theta) P_l(\cos\theta') \right]$$
$$= \frac{1}{2} \left[\sum_{l=1}^{\infty} 2l g^l P_l(\mu) P_l(\mu') + \sum_{l=0}^{\infty} g^l P_l(\mu) P_l(\mu') \right].$$
$$(A7)$$

Using the orthogonal relation $\int_{-1}^{1} P_l(\mu) P_{l'}(\mu) d\mu = (2/2l + 1)\delta_{l,l'}$, we have

$$R_0(g) = \frac{1}{2} \int_{-1}^{1} d\mu \int_{-1}^{1} d\mu' R^d(\mu, \mu') = 1, \quad (A8)$$

for which only the term $l = 0$ in Equation (A7) contributes. Similarly,

$$R_1(g) = \frac{1}{2} \int_{-1}^{1} d\mu \int_{-1}^{1} d\mu' \mu R^d(\mu, \mu')$$
$$= \frac{1}{2} \int_{-1}^{1} d\mu \int_{-1}^{1} d\mu' \mu' R^d(\mu, \mu') = 0, \quad (A9)$$

$$R_2(g) = \frac{1}{2} \int_{-1}^{1} d\mu \int_{-1}^{1} d\mu' \mu\mu' R^d(\mu, \mu') = \frac{g}{3}. \quad (A10)$$

These results are used in deriving Equations (9) and (10).

APPENDIX B

NUMERICAL ALGORITHM

To solve Equations (9) and (10) as a system, our computational domain is $(r, x) \in [0, r_{\max}] \times [x_{\text{left}}, x_{\text{right}}]$, where $r_{\max}$, x_{left}, and x_{right} are chosen such that the solution vanishes to zero outside the boundaries. We choose mesh sizes with grid refinement tests to ensure proper numerical resolution. In the following, we describe numerical techniques involved in our algorithm, including approximations to spatial derivatives, numerical boundary condition, and time evolution.

B.1. The WENO Algorithm: Approximations to the Spacial Derivatives

The spacial derivative terms in Equations (9) and (10) are approximated by a fifth-order finite difference WENO scheme.

We first give the WENO reconstruction procedure in approximating $\partial j / \partial x$,

$$\frac{\partial j(\eta^n, r_i, x_j)}{\partial x} \approx \frac{1}{\Delta x}(\hat{h}_{j+1/2} - \hat{h}_{j-1/2})$$

with fixed $\eta = \eta^n$ and $r = r_i$. The numerical flux $\hat{h}_{j+1/2}$ is obtained by the fifth-order WENO approximation in an upwind fashion, because the wind direction is fixed. Denote

$$h_j = j(\eta^n, r_i, x_j), \quad j = -2, -1, \ldots, N+3$$

with fixed n and i. The numerical flux from the WENO procedure is obtained by

$$\hat{h}_{j+1/2} = \omega_1 \hat{h}^{(1)}_{j+1/2} + \omega_2 \hat{h}^{(2)}_{j+1/2} + \omega_3 \hat{h}^{(3)}_{j+1/2},$$

where $\hat{h}^{(m)}_{j+1/2}$ are the three third-order fluxes on three different stencils given by

$$\hat{h}^{(1)}_{j+1/2} = -\frac{1}{6}h_{j-1} + \frac{5}{6}h_j + \frac{1}{3}h_{j+1},$$

$$\hat{h}^{(2)}_{j+1/2} = \frac{1}{3}h_j + \frac{5}{6}h_{j+1} - \frac{1}{6}h_{j+2}, \text{ and}$$

$$\hat{h}^{(3)}_{j+1/2} = \frac{11}{6}h_{j+1} - \frac{7}{6}h_{j+2} + \frac{1}{3}h_{j+3}.$$

The nonlinear weights ω_m are given by

$$\omega_m = \frac{\breve{\omega}_m}{\sum_{l=1}^3 \breve{\omega}_l}, \quad \breve{\omega}_l = \frac{\gamma_l}{(\epsilon + \beta_l)^2},$$

where ϵ is a parameter to avoid the denominator becoming zero and is taken as $\epsilon = 10^{-8}$. The linear weights γ_l are given by

$$\gamma_1 = \frac{3}{10}, \quad \gamma_2 = \frac{3}{5}, \quad \gamma_3 = \frac{1}{10},$$

and the smoothness indicators β_l are given by

$$\beta_1 = \frac{13}{12}(h_{j-1} - 2h_j + h_{j+1})^2 + \frac{1}{4}(h_{j-1} - 4h_j + 3h_{j+1})^2,$$

$$\beta_2 = \frac{13}{12}(h_j - 2h_{j+1} + h_{j+2})^2 + \frac{1}{4}(h_j - h_{j+2})^2,$$

$$\beta_3 = \frac{13}{12}(h_{j+1} - 2h_{j+2} + h_{j+3})^2 + \frac{1}{4}(3h_{j+1} - 4h_{j+2} + h_{j+3})^2.$$

To approximate the r-derivatives in the system of Equations (9) and (10), we need to perform the WENO procedure based on a characteristic decomposition. We write the left-hand side of Equations (9) and (10) as

$$\mathbf{u}_t + A\mathbf{u}_r,$$

where $\mathbf{u} = (j, f)^T$ and

$$A = \begin{pmatrix} 0 & 1 \\ \frac{1}{3} & 0 \end{pmatrix}$$

is a constant matrix. To perform the characteristic decomposition, we first compute the eigenvalues, the right eigenvectors, and the left eigenvectors of A and denote them by Λ, R, and R^{-1}. We then project $\mathbf{u}$ to the local characteristic fields $\mathbf{v}$ with $\mathbf{v} = R^{-1}\mathbf{u}$. Now $\mathbf{u}_t + A\mathbf{u}_r$ of the original system is decoupled as two independent equations as $\mathbf{v}_t + \Lambda\mathbf{v}_r$. We approximate the derivative $\mathbf{v}_r$ component by component, each with the correct upwind direction, with a WENO reconstruction procedure similar to the procedure described above for $\partial j / \partial x$. In the end, we transform $\mathbf{v}_r$ back to the physical space by $\mathbf{u}_r = R\mathbf{v}_r$. We refer readers to Cockburn et al. (1998) for more implementation details.

B.2. Numerical Boundary Condition

To implement the boundary condition (Equation (12)), we also need to perform a characteristic decomposition as discussed above. Using the same notation as before, we project $\mathbf{u}$ to the local characteristic fields $\mathbf{v}$ with $\mathbf{v} = R^{-1}\mathbf{u}$. Denote $\mathbf{v} = (v_1, v_2)^T$; now $\mathbf{u}_t + A\mathbf{u}_r$ of the original system is decoupled to two independent scalar operators given by

$$\frac{\partial v_1}{\partial t} + \lambda_1 \frac{\partial v_1}{\partial r}; \quad \frac{\partial v_2}{\partial t} + \lambda_2 \frac{\partial v_2}{\partial r},$$

where $\lambda_1 = \sqrt{3}/3$ and $\lambda_2 = -\sqrt{3}/3$. The characteristic line starting from the boundary $r = r_{\max}$ for the first equation is pointing outside the computational domain while the one for the second equation it is pointing inside. For "well-posedness" of our system, we need to impose the boundary condition there as

$$v_2 = \alpha v_1 + \beta,$$

with constants α and β. We can calculate the values of α and β based on Equation (12) and the left and right eigenvectors of A. For example, if we take

$$R = \begin{pmatrix} \frac{\sqrt{3}}{2} & \frac{\sqrt{3}}{2} \\ \frac{1}{2} & -\frac{1}{2} \end{pmatrix},$$

we can compute that $\alpha = 7 - 4\sqrt{3}$ and $\beta = 0$. We use extrapolation to obtain the value of v_1 and then compute the value v_2. In the end, we transfer $\mathbf{v}$ back to the physical space by $\mathbf{u} = R\mathbf{v}$.

B.3. Time Evolution

To evolve in time, we use the third-order total variation diminishing Runge–Kutta time discretization (Shu & Osher 1988). For the system of ordinary differential equations $u_t = L(u)$, the third-order Runge–Kutta method is

$$u^{(1)} = u^n + \Delta\tau L(u^n, \tau^n),$$

$$u^{(2)} = \frac{3}{4}u^n + \frac{1}{4}(u^{(1)} + \Delta\tau L(u^{(1)}, \tau^n + \Delta\tau)),$$

$$u^{n+1} = \frac{1}{3}u^n + \frac{2}{3}(u^{(2)} + \Delta\tau L(u^{(2)}, \tau^n + \frac{1}{2}\Delta\tau)).$$

REFERENCES

Adams, T. F. 1972, ApJ, 174, 439
Adams, T. F. 1975, ApJ, 201, 350
Adams, T. F., Hummer, D. G., & Rybicki, G. B. 1971, J. Quant. Spectrosc. Radiat. Transfer, 11, 1365
Avery, L. W., & House, L. L. 1968, ApJ, 152, 493
Blanc, G. A., Adams, J. J., Gebhardt, K., et al. 2011, ApJ, 736, 31
Bonilha, J. R. M., Ferch, R., Salpeter, E. E., Slater, G., & Noerdlinger, P. D. 1979, ApJ, 233, 649
Cockburn, B., Johnson, C., Shu, C.-W., & Tadmor, E. 1998, in Advanced Numerical Approximation of Nonlinear Hyperbolic Equations, ed. A. Quarteroni (Lecture Notes in Mathematics, Vol. 1697; Berlin: Springer), 450
Dijkstra, M., Haiman, Z., & Spaans, M. 2006, ApJ, 649, 14
Dijkstra, M., & Loeb, A. 2009, MNRAS, 400, 1109
Draine, B. T. 2003, ApJ, 598, 1017
Draine, B. T., & Lee, H. M. 1984, ApJ, 285, 89
Fang, L. Z. 2009, Int. J. Mod. Phys. D, 18, 1943
Fardal, M. A., Katz, N., Gardner, J. P., et al. 2001, ApJ, 562, 605
Field, G. B. 1958, Proc. IRE, 46, 240
Field, G. B. 1959, ApJ, 129, 551
Haiman, Z., & Spaans, M. 1999, ApJ, 518, 138
Haiman, Z., Spaans, M., & Quataert, E. 2000, ApJ, 537, L5
Hansen, M., & Oh, S. P. 2006, MNRAS, 367, 979
Harrington, J. P. 1973, MNRAS, 162, 43
Hayes, M., Östlin, G., Schaerer, D., et al. 2010, Nature, 464, 562
Hayes, M., Schaerer, D., Östlin, G., et al. 2011, ApJ, 730, 8
Henyey, L. G., & Greenstein, J. L. 1941, AJ, 93, 70
Hummer, D. G. 1962, MNRAS, 125, 21
Hummer, D. G. 1965, Mem. R. Astron. Soc., 70, 1
Hummer, D. G. 1969, MNRAS, 145, 95
Hummer, D. G., & Kunasz, P. B. 1980, ApJ, 236, 609
Jiang, G., & Shu, C.-W. 1996, J. Comput. Phys., 126, 202
Latif, M., Schleicher, D. R. G., Spaans, M., & Zaroubi, S. 2011, MNRAS, 413, L33
Laursen, P., Sommer-Larsen, J., & Andersen, A. 2009, ApJ, 704, 1640
Li, A., & Draine, B. T. 2001, ApJ, 550, L213
Liu, J., Qiu, J.-M., Feng, L.-L., Shu, C.-W., & Fang, L.-Z. 2007, ApJ, 663, 1
Neufeld, D. A. 1990, ApJ, 350, 216
Neufeld, D. A. 1991, ApJ, 370, L85
Osterbrock, D. E. 1962, ApJ, 135, 195
Pei, Y. C. 1992, ApJ, 395, 130
Qiu, J.-M., Feng, L.-L., Shu, C.-W., & Fang, L.-Z. 2006, New Astron., 12, 1
Qiu, J.-M., Feng, L.-L., Shu, C.-W., & Fang, L.-Z. 2007, New Astron., 12, 398
Qiu, J.-M., Shu, C.-W., Liu, J.-R., & Fang, L.-Z. 2008, New Astron., 13, 1
Roy, I., Qiu, J.-M., Shu, C.-W., & Fang, L.-Z. 2009a, New Astron., 14, 513
Roy, I., Shu, C.-W., & Fang, L. Z. 2010, ApJ, 716, 604
Roy, I., Xu, W., Qiu, J.-M., Shu, C.-W., & Fang, L.-Z. 2009b, ApJ, 694, 1121
Roy, I., Xu, W., Qiu, J.-M., Shu, C.-W., & Fang, L.-Z. 2009c, ApJ, 703, 1992
Rybicki, G. B. 2006, ApJ, 674, 709
Rybicki, G. B., & Dell'Antonio, I. P. 1994, ApJ, 427, 603
Rybicki, G. B., & Lightman, A. P. 1979, Radiative Processes in Astrophysics (New York: Wiley)
Shu, C.-W., & Osher, S. 1988, J. Comp. Phys., 77, 439
Spaans, M., & Silk, J. 2006, ApJ, 652, 902
Spitzer, L., & Greenstein, J. L. 1951, ApJ, 114, 407
Stratta, G., Maiolino, R., Fiore, F., & D'Elia, V. 2007, ApJ, 661, 9
Unno, W. 1955, PASJ, 7, 81
Verhamme, A., Schaerer, D., Atek, H., & Tapken, C. 2008, A&A, 491, 89
Verhamme, A., Schaerer, D., & Maselli, A. 2006, A&A, 460, 397
Weingartner, J. C., & Draine, B. T. 2001, ApJ, 548, 296
Wouthuysen, S. A. 1952, AJ, 57, 31
Xu, W., & Wu, X.-P. 2010, ApJ, 710, 1432